Moiré fractals in twisted graphene layers

Deepanshu Aggarwal, Rohit Narula, and Sankalpa Ghosh
Department of Physics, Indian Institute of Technology Delhi, Hauz Khas, New Delhi 110016
(Dated: June 8, 2023)

Twisted bilayer graphene (TBLG) subject to a sequence of commensurate external periodic potentials reveals the formation of moiré fractals that share striking similarities with the central place theory (CPT) of economic geography, thus uncovering a remarkable connection between twistronics and the geometry of economic zones. The moiré fractals arise from the self-similarity of the hierarchy of Brillouin zones (BZ) so formed, forming a nested subband structure within the bandwidth of the original moiré bands. The fractal generators for TBLG under these external potentials are derived and we explore their impact on the hierarchy of the BZ edges. Furthermore, we uncover parallels between the modification of the BZ hierarchy and magnetic BZ formation in the Hofstadter butterfly, allowing us to construct an incommensurability measure for moiré fractals as a function of the twist angle. The resulting band structure hierarchy bolsters correlation effects, pushing more bands within the same energy window for both commensurate and incommensurate structures.

Fractals are ubiquitous, spanning from the natural fractals of Romanesco broccoli to abstract fractals such as the Mandelbrot set [1, 2]. These structures display an infinite nesting pattern, with parts that vary in concentration, demonstrating self-similarity across different analytical scales. Iterated function systems (IFSs) are a common and general way of generating fractals. Many unusual geometries turn out to be the attractor [3] of these IFSs, such as the Koch curve. The procedure of generating such iterated fractals involves a generator and a starting shape that is called an initiator. The generator is then applied to the initiator recursively, which finally provides the associated attractor. Of particular interest in this work are iterated fractals whose key features are embedded in the quadratic equation

$$x^2 + \beta x - \left(L_N - \beta^2\right)/3 = 0, \tag{1}$$

where for a natural number β if (1) has a discriminant $\mathcal{D} \in \mathbb{Z}$, L_N forms a set of natural numbers generating the points of a triangular lattice with integral coordinates [4] as shown in FIG. 1(a). Therein the intersections of $x \in \mathbb{Z}^+$ lines parallel to the Y-axis, with the β lines that are parallel to $X = Y$ (corresponding to $\beta = 0$) give the coordinates of the location of the L_N. β can be interpreted as the distance of the β-rays from the $X = Y$-line, while L_N uniquely characterize the intersection points of the x and β-rays.

In this work we show that for a given L_N and β combination, Eq.(1) describes an emergent fractality when commensurate or incommensurate moiré patterns in twisted bilayer graphene (TBLG) [6–34] are subjected to a sequence of periodic potentials as shown in FIG. 1(b), having the same moiré periodicity of the structures on which they are applied, but rotated (twisted) relatively by a specific angle that restores the commensuration between the applied potential and the subjected structure. The edges of the first Brillouin zone (FBZ) formed in this sequential process at each iteration form a fractal (see for example FIGS. 3, 5) whose dimensions are determined by L_N, which in this case is the number of unit cells in a newly formed BZ which fits a unit cell of the preceding BZ at each iteration. The shape of the corresponding fractal generator is determined by β.

We also demonstrate that the emergent fractality described by Eq.(1) which arises from the application of the sequence of superlattice potentials is geometrically similar to the hierarchy and fractality observed in the central place theory (CPT) of economic geography used to describe the economically-motivated agglomeration of trade zones around human settlements, pioneered by Walter Christaller [35] and subsequently by Augustine Lösch [36]. The link between the aforementioned geometric fractals in the context of moiré

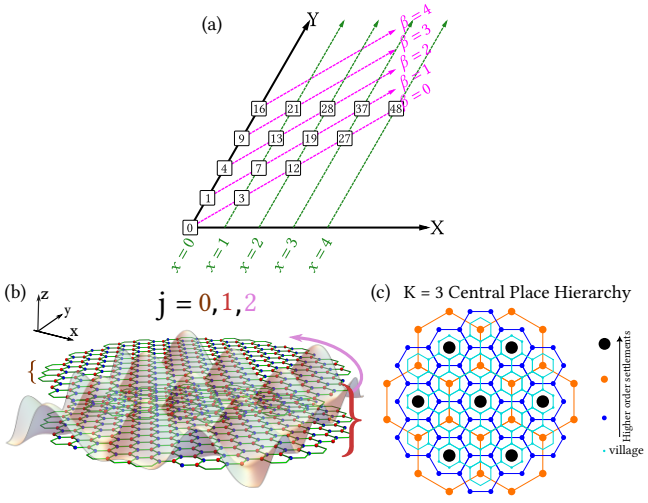

FIG. 1: (a) Shows the quantities L_N, β and x over a triangular coordinate system (the X- and Y-axis are tilted at 60° with each other). β identifies the line along which a given Löschian number L_N exists and the x-lines give the x-coordinates. This scheme also classifies the different types of commensurate structures as described in the text. (b) The real-space creation of each iteration is shown. TBLG is created by stacking graphene layers, with the top layer being the zeroth iteration $j = 0$ and the bottom layer being the next iteration $j = 1$. The subsequent iteration, *i.e.*, $j = 2$ is created by applying a z-independent external periodic potential identically to both the graphene layers. (c) Shows the $K = 3$ central place hierarchy (since a hexagon of each layer encloses three hexagons of an adjacent layer) where each layer corresponds to a particular order of settlement [5]. In the present work L_N plays the role of K.

band engineering and the geometry of CPT becomes apparent when a relatively large net of densely packed hexagonal trade areas, where each hexagon is centered on a large settlement, is stacked on other nets with hexagonal cells of fixed area within a layer, but with trade areas varying from layer to layer such that each smaller trade area represents smaller settlements [35–41] as shown in FIG. 1(c). This draws a close analogy with the well known Hofstadter butterfly [42, 43] which provides a theory describing the topological origins of the quantum Hall effect through the ground-breaking work of TKNN [44, 45]. We exploit this analogy to construct a measure of incommensuration for such a moiré structure. In the CPT literature L_N were termed as the Löschian numbers (LN) [46]. We shall demonstrate that the application of a sequence of moiré potentials on TBLG, forms a CPT fractal off its hierarchy of BZ edges, and substantiate these findings via the microscopic model of TBLG and present our results.

The rapid progress in the fabrication of two-dimensional (2D) layered materials such as TBLG has stimulated interest in the study of the effect of substrates [47–50]. These may be considered as perturbations to TBLG via an external periodic potential [51–53]. The application of a sequence moiré external potentials (mEP) to TBLG (FIG. 1(a)) leads to a commensurate structure between the mEP at each j-th iteration and the TBLG with all the potentials upto the $(j-1)$-th iteration. The Hamiltonian considered for the j-th level of iteration is

$$H_j = \begin{pmatrix} \hat{h}_{\boldsymbol{k}}(\theta/2) + \sum_{i=1}^{j} V_i(\boldsymbol{r}) & T(\boldsymbol{r}) \\ T^{\dagger}(\boldsymbol{r}) & \hat{h}_{\boldsymbol{k}}(-\theta/2) + \sum_{i=1}^{j} V_i(\boldsymbol{r}) \end{pmatrix} \tag{2}$$

In the diagonal, $\hat{h}_{\boldsymbol{k}}(\theta) = v_F\, \boldsymbol{\sigma}_\theta \cdot \left(\hat{\boldsymbol{k}} - \boldsymbol{K}^{\theta}\right)$ is the Hamiltonian [54] of pristine graphene rotated by an angle θ, where v_F [55] is the Fermi velocity, and $\boldsymbol{K}^{\theta}$ is the wave vector of the rotated Dirac point in the right valley. The transformed Pauli matrices $\boldsymbol{\sigma}_\theta = e^{-i\sigma_z\theta/2}\left(\sigma_x, \sigma_y\right) e^{i\sigma_z\theta/2}$ account for the rotation. The spatially dependent interlayer hopping matrix is $T(\boldsymbol{r}) = \sum_{i=1,2,3} T_i\, e^{-i\boldsymbol{q}_i\cdot\boldsymbol{r}}$, where the $\boldsymbol{q}$-vectors are the basis vectors of the moiré Brillouin zone (mBZ) of the TBLG. The coefficient matrices in the interlayer coupling matrix $T(\boldsymbol{r})$ are the interlayer tunneling matrices [10, 56–58]. The external potential $V_j(\boldsymbol{r})$ is periodic as $V(\boldsymbol{r} + n_1\,\boldsymbol{t}_1^j + n_2\,\boldsymbol{t}_2^j) = V_j(\boldsymbol{r})$, where the two primitive vectors are $\boldsymbol{t}_i^{(j)} = [\mathcal{R}(\theta)]\ \boldsymbol{a}_i^{(j-1)}$ for both $i = 1, 2$. Here $\theta = \theta_r$ corresponds to the specific twist angle between the moiré pattern and the external potential and at which the commensurability of the resulting structure is restored. The 2×2 matrix $\mathcal{R}(\theta_r)$ is a two-dimensional rotation matrix at these commensurate twist angles. The condition for commensuration under such rotation that maps an integer pair $\{n_1, n_2\}$ to $\{m_1, m_2\}$, both in the unit of lattice vectors, becomes

$$\begin{pmatrix} m_1 \\ m_2 \end{pmatrix} = \begin{pmatrix} \cos(\theta_r) - \epsilon\cot(\phi)\sin(\theta_r) & -\epsilon\frac{a_2^{(j-1)}}{a_1^{(j-1)}\sin(\phi)}\sin(\theta_r) \\ \epsilon\frac{a_1^{(j-1)}}{a_2^{(j-1)}\sin(\phi)}\sin(\theta_r) & \cos(\theta_r) + \epsilon\cot(\phi)\sin(\theta_r) \end{pmatrix} \begin{pmatrix} n_1 \\ n_2 \end{pmatrix} \tag{3}$$

where $\epsilon = \mathrm{sgn}\left[\left(\boldsymbol{a}_1^{(j-1)} \times \boldsymbol{a}_2^{(j-1)}\right)_z\right]$, $a_1^{(j-1)} = \left|\boldsymbol{a}_1^{(j-1)}\right|$ and $a_2^{(j-1)} = \left|\boldsymbol{a}_2^{(j-1)}\right|$ and ϕ is the angle between $\boldsymbol{a}_1^{(j-1)}$ and $\boldsymbol{a}_2^{(j-1)}$. When the basic lattice structure is hexagonal, $a_1^{(j-1)} = a_2^{(j-1)}$ and $\phi = \pi/3$. For integer solutions m_1, m_2, n_1 and n_2, the necessary and sufficient condition demands these matrix elements to assume only rational values [11, 59], thus leading to a set of Diophantine equations.

In the process of creating this sequence of potentials as shown in FIG. 1, the potential $V_1(\boldsymbol{r}) = 0$ at the first iteration, $j = 1$ is such that H_1 in (2) becomes the standard Hamiltonian of the TBLG while the potentials for $j \geq 2$ are non-zero. For the next iteration $j = 2$, the potential $V_2(\boldsymbol{r})$ is periodic with primitive vectors $\boldsymbol{t}_i^{(2)} = [\mathcal{R}(\theta_r)]\,\boldsymbol{a}_i^c$ for $i = 1, 2$, where $\boldsymbol{a}_i^c$ are the primitive vectors of the commensurate TBLG. The solution of Eq. (3) by mapping a lattice point (n_1, n_2) of the lattice spanned by the primitive vectors $\left\{\boldsymbol{a}_1^c, \boldsymbol{a}_2^c\right\}$ to the point (m_1, m_2) of the lattice spanned by the primitive vectors of the potential $\left\{\boldsymbol{t}_1^{(2)}, \boldsymbol{t}_2^{(2)}\right\}$ provides the primitive vectors of their commensuration, *i.e.*, $\left\{\boldsymbol{a}_1^{(2)}, \boldsymbol{a}_2^{(2)}\right\}$. Following a similar procedure, the potential $V_j(\boldsymbol{r})$ at the jth-level of iteration for $j \geq 2$ is periodic with vectors $\boldsymbol{t}_i^{(j)} = [\mathcal{R}(\theta_r)]\,\boldsymbol{a}_i^{(j-1)}$. At this stage the commensurate structure of the potential $V_j(\boldsymbol{r})$ and the structure upto the $(j-1)$th-level is spanned by the vectors $\left\{\boldsymbol{a}_1^{(j)}, \boldsymbol{a}_2^{(j)}\right\}$. To see the consequences of this stack of external potentials a simple cosine potential with only six Fourier components is employed as,

$$V_i(\boldsymbol{r}) = 2V_0\left[\cos\left(\boldsymbol{G}_1^{(i)}\cdot\boldsymbol{r}\right) + \cos\left(\boldsymbol{G}_2^{(i)}\cdot\boldsymbol{r}\right) + \cos\left(\boldsymbol{G}_3^{(i)}\cdot\boldsymbol{r}\right)\right] \tag{4}$$

where $\boldsymbol{G}_3^{(i)} = -\boldsymbol{G}_1^{(i)} - \boldsymbol{G}_2^{(i)}$ and $\boldsymbol{G}_1^{(i)}$ and $\boldsymbol{G}_2^{(i)}$ are the reciprocal-lattice vectors which are defined such that $\boldsymbol{t}_i^{(j)} \cdot$

$\boldsymbol{G}_k^{(j)} = 2\pi\delta_{ik}\ \forall\ i,k = 1,2$ and V_0 is the strength of the potential. It has been pointed out that the intrinsic Coulomb interactions can be modeled using such an onsite mEP having the same periodicity as that of the moiré pattern [60–63] at least as a starting *ansatz* for a self-consistent calculation.

Eq. (3) demonstrates that each commensuration of either TBLG or TBLG plus the mEPs is characterized by two integers (q,p), where $q \geq p > 0$ are each co-prime. Each (q,p) leads to an L_N given by (for details see appendix)

$$L_N = \frac{\left|\boldsymbol{b}_1^{(j-1)} \times \boldsymbol{b}_2^{(j-1)}\right|}{\left|\boldsymbol{b}_1^{(j)} \times \boldsymbol{b}_2^{(j)}\right|} = p_1^2 + p_2^2 + p_1\, p_2 \tag{5}$$

where $\boldsymbol{b}_i^{(j)}$ are the reciprocal-lattice vectors that are defined as $\boldsymbol{a}_i^{(j)} \cdot \boldsymbol{b}_k^{(j)} = 2\pi\delta_{ik}\ \forall\ i,k = 1,2$ and $p_1 = p_1(p,q)$ and $p_2 = p_2(p,q)$ which are both positive integers. For the considered a hexagonal lattice structure, the integer p_2 can be written as $p_1 + \beta$ such that L_N with $\beta = 0$ lie on the $X = Y$ line and the numbers with $\beta > 0$ lie on the lines that are parallel to $X = Y$ as shown in FIG. 1(a). This substitution converts Eq. (5) straightforwardly into Eq.(1). Thus each L_N lies on an intersection point of the x- and β-rays as shown in FIG. 1(a) such that the corresponding values of x and β of the intersection points satisfy Eq. (1). For each L_N and some β, the cardinal number n_c of an iterated function system $W = \{w_n : n = 1,2,\ldots,n_c\}$ (IFS) is obtained using L_N and β, where w_n are defined as the affine transformations. For the present case, the BZ of SLG (one of the constituting layers in TBLG) is the initiator A_0. The application of W on one side of A_0 results in the corresponding *fractal* generator (FG). When this FG is applied to each arm of A_0, it generates the edge of the successive BZ and the recursive process is continued to generate a sequence of such BZs. Ideally, when this process of applying the FG is performed up to infinity, it leads to a limiting structure that is known as *attractor* (A). This is how the moiré fractal (attractor A), which is also a CPT fractal, is generated.

The hierarchical construct that theorises economic activity in CPT: L_N, depicts successively smaller regions contained in a given trade area at each stage of the sequence. Subsequent analysis [64] provided a number theory-based method to identify conditions for arbitrary natural numbers L_N, satisfying the properties as demanded by Eq. (1). This led to a correspondence between a partition of the central place lattice and a quadratic form (1) that allows the systematic determination of the lattice coordinates where economic zones are located, and consequently the fractal generator that generates the entire central place hierarchy corresponding to that number. In the subsequent discussion we shall deliberate on the properties of such fractal generators for specific cases of TBLG in the presence of specific mEPs.

We begin with the corresponding transformation mappings of the fractal generator corresponding to $q = 3$ and $p = 1$ and for $q = 2, p = 1$. A more diverse list of such fractal generators are provided in the appendix in (Table-I) [65] and with additional discussion. The first case corresponds to the commensurate angle $\theta \sim 21.79°$ which has been recently explored experimentally for pristine TBLG in [66]. The integers q,p are found to be $3,1$ from (3), respectively. Consequently, one can evaluate the number $L_N = 7$ from (5) which lies at the intersection of the x-ray $x = 1$ and the β-ray with $\beta = 1$ as shown in FIG. 1(a). Corresponding to these L_N and β, the cardinal number of the IFS is obtained as $n_c = 3$. Therefore, the IFS is $W = \{w_1, w_2, w_3\}$, where each of the w's are given as

$$w_1 = \mathcal{R}(-\phi_1)\frac{\mathcal{I}}{s};\quad w_2 = \mathcal{R}(\phi_2)\frac{\mathcal{I}}{s} + w_1;\quad w_3 = w_1 + w_2 \tag{6}$$

where $s = \sqrt{L_N}$ is the *contractivity* factor, defined as the ratio $\left|\boldsymbol{b}^{(j-1)}\right| / \left|\boldsymbol{b}^{(j)}\right|$. For $p_1 = 1$, $p_2 = 2$ and $s = \sqrt{7}$, the two angles are $\phi_1 = \cos^{-1}\left(\frac{2p_1+p_2}{2s}\right)$ and $\phi_2 = \frac{\pi}{3} - \phi_1$ and $\mathcal{I}$ is a 2×2 identity matrix. The fractal dimension D_f of the attractor A is obtained using L_N as $D_f = \log(n_c)/\log(s)$ [1]. Their action on the initiator can be understood by first choosing one of the sides of the initiator, while letting it be the side of the BZ of SLG rotated clockwise with the angle $\theta/2 \sim 10.89°$. The corresponding vector in reciprocal space is

$$\boldsymbol{u} = \frac{1}{3}\left(2\boldsymbol{b}_1^{-\theta/2} + \boldsymbol{b}_2^{-\theta/2}\right) \equiv \begin{bmatrix} u_x \\ u_y \end{bmatrix} \tag{7}$$

where $\boldsymbol{b}_1^{-\theta/2}$ and $\boldsymbol{b}_1^{-\theta/2}$ are the two reciprocal lattice vectors of the rotated graphene layers. *E.g.*, mapping w_1 shortens the length of the vector $\boldsymbol{u}$ by $s = \sqrt{7}$ times and rotates the vector clockwise by an angle $\cos^{-1}\left(2/\sqrt{7}\right)$, that provides the first side of the FG, namely $\boldsymbol{u}_1$. The three successive mappings giving the three sides of the FG can now be simply given by $\boldsymbol{u}_{1,2,3} = w_{2,3}\boldsymbol{u}$. The full process is depicted in FIG. 2(a). The second case corresponds to the commensuration $\theta \sim 32.20°$ with $q = 2$ and $p = 1$, for which $L_N = 13$ and the cardinal number of an IFS is $n_c = 5$. Considering the side of the initiator to be identical to the vector $\boldsymbol{u}$ in Eq.(7) as shown in FIG. 2(b), the affine transformations become

$$w_1 = \mathcal{R}\left(\phi_1\right)\frac{\mathcal{I}}{s};\quad w_2 = \mathcal{R}(-\phi_2)\frac{\mathcal{I}}{s} + w_1$$
$$w_3 = w_1 + w_2;\quad w_4 = w_2 + w_3;\quad w_5 = \mathcal{R}(-(\frac{\pi}{3} + \phi_2))\frac{\mathcal{I}}{s} + w_4 \tag{8}$$

where $p_1 = 1$, $p_2 = 3$ and $s = \sqrt{13}$ is the contractivity factor.

We shall now illustrate the consequences of the above construction by applying them directly to the band structure of the commensurate TBLG subjected to the hierarchical mEPs described by the Hamiltonian (2). The FIGS. 3(a1) and (b1) show the superimposed BZs corresponding to first three iterations $j = 1,2,3$ formed by the hierarchical moiré potential applied to the two commensurate structures at $\theta = \theta_r \sim 21.786°$ and $\theta = \theta_r \sim 32.204°$. The shape of the fractal generators are shown in the next column. For both the structures, the generator is applied alternatingly outside and inside of the edges of the corresponding initiators (shown by

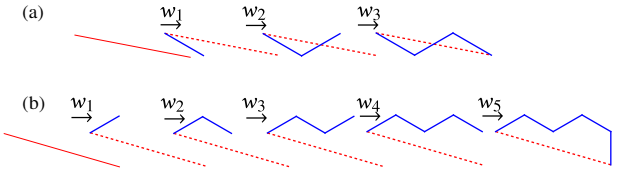

FIG. 2: The stepwise creation of the FG corresponding to (a) $L_N = 7$ with $q = 3$ and $p = 1$, and (b) the number $L_N = 13$ with $q = 2$ and $p = 1$.

red dashed lines in both the Figs.3(a2) and (b2)), and it shows the emerging fractality for both the structures with fractal dimensions $D_f = 1.129$ and $D_f = 1.174$. The magnitude of the reciprocal lattice vectors ($i = 1, 2$) constitute the Cauchy sequence [67], i.e.,

$$\lim_{j\to\infty}\left\{\frac{\left|\boldsymbol{b}_1^{\pm\theta/2}\right|}{s^{(j-1)}}\right\}\to 0 \tag{9}$$

where the convergence rate depends on the values of q and p. The insets adjacent to the BZs of both the figures show the convergence of the Cauchy sequence in reciprocal space by the solid blue lines and consequently the divergence of the magnitude of real-space lattice vectors by the solid red lines.

In the presence of a rotated mEP at the j-th iteration on a commensurate TBLG at $(j-1)$-th iteration described by the Hamiltonian (2), the lattice translation operators (TOs) corresponding to the primitive vectors of the $(j-1)$-th iteration do not commute with the Hamiltonian. The commuting TOs at the j-th iteration need to be redefined through Eq. 5 corresponding to the two primitive vectors $\boldsymbol{a}_1^c = p_1\boldsymbol{a}_1 + p_2\boldsymbol{a}_2$ and $\boldsymbol{a}_2^c = -p_2\boldsymbol{a}_1 + (p_1+p_2)\,\boldsymbol{a}_2$ with $p_1, p_2 \in \mathbb{Z}^+$. They satisfy $\hat{T}_{\boldsymbol{a}_1^c}\hat{T}_{\boldsymbol{a}_2^c} = \hat{T}_{\boldsymbol{a}_2^c}\hat{T}_{\boldsymbol{a}_1^c}$. This leads to large real-space supercell at the j-th iteration and a more squeezed BZ scaled by the contractivity factor defined earlier, and are depicted in FIG. 3(a1) and (b1). This is conventionally referred to as a *mini* zone (MZ) [50, 68].

To draw the parallel with the problem of the Hofstadter butterfly that considers the Bloch electrons in a transverse magnetic field, we note that the magnetic translation operators (MTOs) do not commute with each other in general giving $\hat{T}_{\boldsymbol{a}_1}\hat{T}_{\boldsymbol{a}_2} \neq \hat{T}_{\boldsymbol{a}_2}\hat{T}_{\boldsymbol{a}_1}$, where $\boldsymbol{a}_1$ and $\boldsymbol{a}_2$ are the two direct lattice primitive vectors of the underlying lattice. To preserve the commutativity, an enlarged magnetic unit cell is considered such that the MTOs corresponding to new Bravais lattice vectors commute, $\hat{T}_{\boldsymbol{a}_1'}\hat{T}_{\boldsymbol{a}_2'} = \hat{T}_{\boldsymbol{a}_2'}\hat{T}_{\boldsymbol{a}_1'}$. There, the dimensionless quantity $\Phi/\Phi_0 = |\boldsymbol{a}_1\times\boldsymbol{a}_2|/l_B^2$ where Φ is the magnetic flux per plaquette, $\Phi_0 = \hbar/e$, namely, and l_B is the magnetic length, define the measure of the incommensurability in presence of a magnetic field which breaks time reversal (TR) symmetry [42, 69, 70]. It is therefore natural to ask, can one define a measure of incommensurability for the case of a commensurate TBLG in a rotated mEP under consideration, where there is no explicit TR symmetry breaking? Accordingly, we define a dimensionless measure of incommensuration, as

$$\frac{\Delta A(\theta)}{A_{\rm FBZ}^{(j-1)}} = \left(1 - \frac{\lfloor A_{\rm FBZ}^{(j-1)}/A_{\rm FBZ}^{(j)}\rfloor}{A_{\rm FBZ}^{(j-1)}/A_{\rm FBZ}^{(j)}}\right) \tag{10}$$

where $A_{\rm FBZ}^{(j)} = \left|\boldsymbol{b}_1^{(j)}\times\boldsymbol{b}_2^{(j)}\right|$ is the area of the first BZ at the jth-iteration, and $\lfloor\ldots\rfloor$ denotes the greatest integer function.

To appreciate the relation (10), we note that the reciprocal lattice vectors of the moiré Brillouin zone (MBZ) can be obtained using the definition of moiré pattern [10, 71, 72] independent of whether the angle is commensurate or not, and is given by the shift between the Dirac points $\Delta\boldsymbol{K} = \boldsymbol{K}^{\theta/2} - \boldsymbol{K}^{-\theta/2}$, where $\boldsymbol{K}^{\pm\theta/2}$ are the wave-vectors of the rotated Dirac points in tBLG. This may or may not coincide with the lattice vectors that result from the solution of the Diophantine equation (3) for the commensurate angles that give the side length of the hexagonal BZ as $(\ell) = \left|\frac{2\boldsymbol{b}_1^c+\boldsymbol{b}_2^c}{3}\right|$ (see FIG. 3(a1) and (b1)). For the cases $p = 1$ and q odd integers, these two definitions coincide. For the corresponding commensurate angles the ratio $A_{\rm FBZ}^{(j-1)}/A_{\rm FBZ}^{(j)}$ is a Löschian number $N \in \mathbb{Z}^+$ and therefore ΔA is identically zero. These corresponds to the blue colored points in FIG. 4. For a generic (q,p), $\Delta\boldsymbol{K} = \begin{cases}\frac{2p}{3\gamma}\left(2\boldsymbol{b}_1^{(j)}+\boldsymbol{b}_2^{(j)}\right) & \text{if } \gcd(p,3)=1\\ \frac{2p}{3\gamma}\boldsymbol{b}_2^{(j)} & \text{if } \gcd(p,3)=3\end{cases}$ where $\gamma = \gcd(3q-p, 3q+p)$ [73]. Accordingly the zeros of $\Delta A/A_{FBZ}^{(j-1)}$ for other commensurate angles make an upward shift by different amounts in FIG. 4. The minima of the V-shaped regions indicates the minimum ΔA in proximity to the different commensurate angles where the ratio becomes rational.

For $q = 2n+1$ for $n = 1, 2, 3, \ldots$ and $p = 1$, the shift $\Delta\boldsymbol{K}$ is always equal to ℓ as shown in FIG. 3(a1) and the moiré lattice vectors coincide with the commensurate cell. Similarly, if $q = 2n$ for $n = 1, 2, 3, \ldots$ with $p = 1$, the shift $|\Delta K| = 2\ell$ as shown in FIG. 3(a1) such that the ratio $A_{\rm FBZ}^{(j)}/A_{\rm FBZ}^{(j-1)}$ takes a value $(4\chi(q)+1)/4$ and therefore the zero of $\Delta A/A_{FBZ}^{(j-1)}$ shifts to $1/(4\chi(q)+1)$, where $\chi(q)$ is some positive integer that depends upon the value of q. It is plotted against the angle θ which is a twist angle or the angle between the tBLG and mEP as shown in FIG. 3(b1).

FIGS. 3(a3) and (b3) show the band structure and corresponding DOS. Precisely L_N number of electronics bands, given by Eq. 5, thrust into the energy bandgap of 7.2 eV for $\theta_r = 21.786°$ and 5.2 eV for $\theta_r = 32.204°$ between the two lowest bands in the absence of mEP at the Γ-point. Whereas the additional bands at the K and K' points confine themselves in the energy range in a even narrower band-gap than the one at Γ-point and the two lowest bands above and below the Fermi energy meet at the Dirac point. In case of incommensurate magic angle TBLG (MATBLG) [7, 10, 74, 75] where the occurrence of flat bands facilitate a variety of correlated phases [20, 21, 76–83], the FG is applied alternatingly outside and inside of the edges of the corresponding initiators which are the mBZ of MATBLG as shown by the red dashed

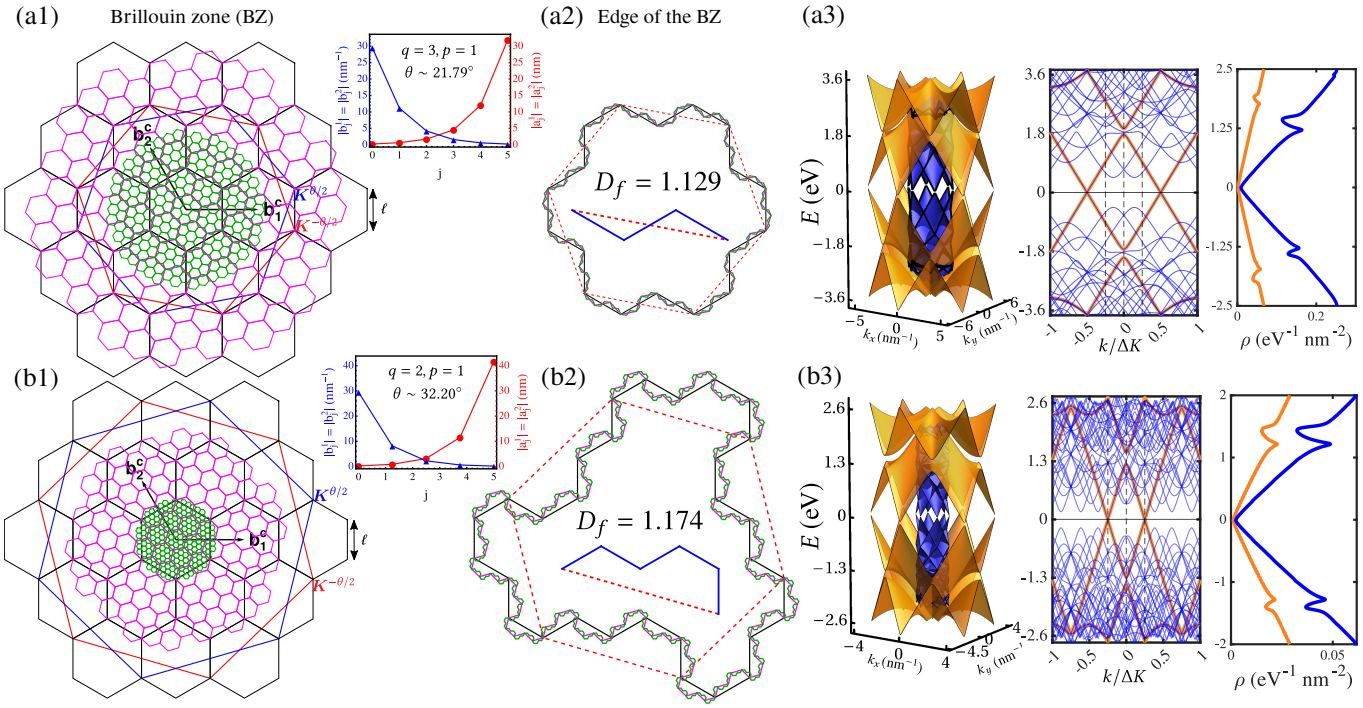

FIG. 3: (a1), (b1) show the Brillouin zone (BZ) corresponding to three successive iterations $j = 1, 2, 3$, with $\{\boldsymbol{b}_1^c, \boldsymbol{b}_2^c\}$ being the reciprocal-lattice primitive vectors corresponding to the $j = 1$ iteration. (a2), (b2) show the fractal structures emerging at the edges of the BZ. In each figure, the dashed red hexagon is the initiator which is the BZ of the SLG rotated clockwise by an angle $\theta/2$. The outer boundary of the fractal structures is shown by the solid blue lines and is created by attaching the generators (shown inside the figure) to the initiator towards the outer and inner region alternatingly. The insets between (a1),(a2) and (b1),(b2) show the magnitude of reciprocal lattice vectors and real-space lattice vectors for $q = 3, p = 1$ and $q = 2, p = 1$, respectively. (a3) and (b3) show the band structures and corresponding density of states (DOS). The shift between the Dirac points for $q = 3$ and $p = 1$ is the same as the side length of the hexagon while the shift ΔK is twice the side length of the hexagon for $q = 2$ and $p = 1$.

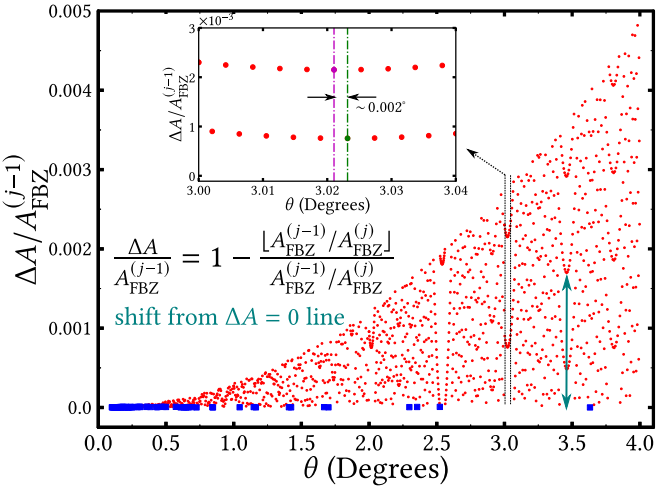

FIG. 4: It shows the incommensuration measure $\Delta A/A_{\rm FBZ}^{(j-1)}$ as a function of the angle θ. The blue rectangles that lie across the zero line indicates the commensurate angles or the angles closest to the commensurate angles for q which is an odd number and $p = 1$. The area of the first BZ in case of incommensurate angles is obtained using the definition of the moiré vectors[72]. The inset confirms that the apparent multivaluedness of the lowest values of the V-like regions at a given value of θ between the two black dashed lines is actually absent and a separation of at least $\sim 0.002°$ exists.

lines in the FIGs. 5(a) and (b). Both these figures also show the superimposed BZs corresponding to the first three iterations $j = 1, 2, 3$ formed by the hierarchical mEP applied to the incommensurate TBLG at the first magic-angle $\theta \sim 1.05°$. FIG. 5(a) corresponds to $\theta_r \sim 13.17°$ and $D_f = 1.093$, whereas FIG. 5(b) corresponds to $\theta_r \sim 21.79°$ and $D_f = 1.129$. The change in D_f and the corresponding Löschian number L_N changes the number of bands that are pushed towards the Fermi level at the Γ-point within a bandgap of ~ 13.76 meV for incommensurate MATLBG to preserve the emerging fractality in a way similar to the case of commensurate structures. Because of the increase of the number of bands to $2N$ within the same bandwidth of MATBLG, the $2(N-1)$ inner bands will now have a significantly reduced curvature as compared to the original flat bands. It can be verified from Fig.(.8) in the appendix that the renormalised Fermi velocity in tBLG in the presence of a hierarchical MEP remains same as in the TBLG even though the Fermi level gets shifted.

In the above calculations we have ignored the lattice relaxation effect in the different region of the graphene bilayer. The non-uniformity in the local AA- and AB/BA-rich regions in TBLG leads to a different perpendicular distance between the constituting layers and therefore the interlayer hopping amplitudes w_0 in local AA/BB-rich regions and w_1 in AB/BA-

rich regions differ. Here we show that the inclusion of corrugation effects in the Hamiltonian (2) does not change the emergent fractality that is linked to the band structures. Using $w_0 = 79.7$ meV and $w_1 = 97.5$ meV [24, 26, 71, 84], the band structures at the first magic angle $\sim 1.05^\circ$ with two angles $\theta_r \sim 21.79^\circ$ and $\theta_r \sim 13.17^\circ$ are shown in the FIG. (6).

The recursive stacking of nets in the CPT framework generates an increasing number of smaller settlements in a given area. Similarly, the recursive moiré potential in a TBLG results in a growing number of electronic bands within a specific energy range, effectively enhancing the correlation effect. Both phenomena can be quantified by the same Löschian numbers L_N. A measure on the effect of this band engineering and emergent fractality due to the mEP on correlation can be understood in terms of the Hubbard parameter ratio $\frac{U}{W}$. It is known that when the Fermi level lies within the flat band, $\frac{U}{W} \gg 1$. At a given iteration under an mEP, $U \longrightarrow \frac{U}{s}$, where $U = e^2\theta/4\pi\kappa\epsilon_0 a$ for the case without any mEP [21], and s is the contractivity factor coming from the FG. Here e is the electron charge and $\kappa = 4$. However now for the closest flat band near the Fermi level, the bandwidth W is reduced by a factor which is significantly larger than s. For example, in FIG. 5(a) the bandwidth is reduced from $\sim$ 6meV to $\sim$ 0.23meV, thereby increasing the ratio $\frac{U}{W} \sim 9$ times as compared to the MATBLG case. The effective mass m^* which scales as $\sqrt{n}/v_F$ at the Fermi level increases as the superlattice density n scales up by the Löschian L_N. For the same reason the density of states (DOS) goes up.

In summary, by considering twisted bilayer graphene subject to a sequence of external potentials, which have the same periodicity of the underlying moiré pattern obtained at an arbitrary angle of twist, but rotated at a given angle, we introduced the notion of moiré fractals and provide a mathematical framework for studying their properties. We underlined how this emergent fractality in the sp^2 carbons found parallels with the CPT of the agglomeration model of trade zones. By comparing the restructuring of the moiré unit cell of the moiré BZ due to this emergent fractality with the formation of magnetic BZ in the well-known Hofstadter butterfly problem, we define a measure of incommensurability in such moiré fractals and demonstrate how they vary as the system goes from an incommensurate to a commensurate structure. Our analysis links the modification of correlation effect with the fractal dimension, implying the possible applications of the moiré fractal. Even though most of our results were obtained using the BM model, we showed that the basic properties of such moiré fractals remain robust even when corrugation effects are included.

A possible route to experimentally imaging moiré fractals is by measuring the differential tunnelling conductance of TBLG subject to the sequence of external potentials at various bias voltages, which may then be compared to the average tunnelling conductance measured on the bare TBLG as was done by Collins *et. al.* in Ref. [85] for Cu (111) decorated with CO molecules who thus created a Penrose till-

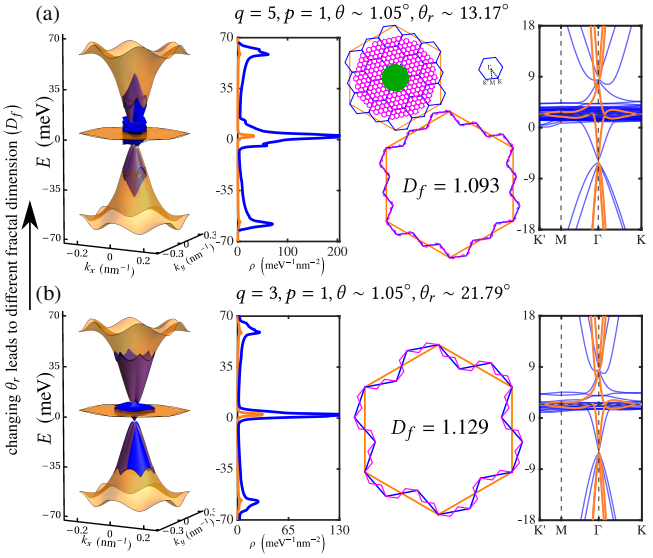

FIG. 5: The band structures at angles $\theta_r \sim 21.79^\circ$ in (a) and $\theta_r \sim 13.17^\circ$ in (b) along the high-symmetry path $K' - M - \Gamma - K$. The twist angle between the layers is the first magic angle $\theta = 1.05^\circ$. The interlayer parameters are chosen as $w_0 = w_1 = 110$ meV and the strength of the potential $V_0 = 1.2$ meV. (left to right) The 3D-band structure is shown where the orange bands are those in the absence of the mEP, while the blue bands include the presence of the mEP. The adjacent figures show the density of states (DOS), the emerged fractal structure in the reciprocal space and lastly, the 2D projection of the bands. Changing the θ_r from (b) to (a) changes the fractal dimension (D_f) , pushing a higher number of bands towards the Fermi level.

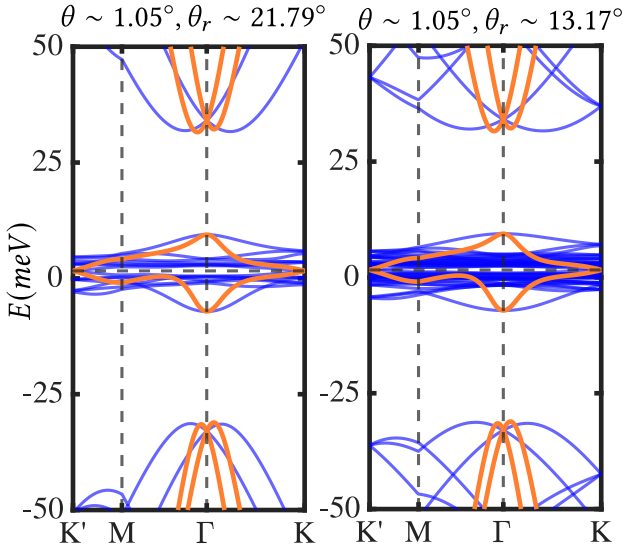

FIG. 6: Inclusion of the corrugation effects by changing the interlayer hopping amplitudes $w_0 = 79.7$ meV and $w_1 = 97.5$ meV does not change the proposed emergence of fractality. The same $2L_N$ bands are quenched within the bandgap of $\sim$ 13 meV.

TABLE I: Each commensuration is characterized uniquely by a pair of coprime-integers (q, p). The Löschian number L_N and the FG are obtained by identifying the number of sides n_c in the generator. The fractal dimension (D_f) corresponding to the various q, p are calculated using L_N and n_c [65]. The outer boundary of the mini-zones superposed over the FBZ of SLG is generated by attaching the fractal generator on a hexagonal initiator.

θ	q	p	L_N	β	n_c	Generator	D_f
21.79°	3	1	7	1	3		1.129
32.20°	2	1	13	2	5		1.093
13.17°	5	1	19	1	5		1.093
38.21°	5	3	7	1	3		1.129
17.90°	11	3	31	4	9		1.280
⋮							

ing [85], and therefore a quasicrystal [85]. In a recent work, quantum twisting microscopy (QTM) was introduced to scan various other van der Waals (vdW) structures [66]. Indeed QTM may be used to image moiré fractals by providing gating to the vdW device at the rotating platform in QTM, giving rise to a rotated mEP [86, 87]. Other higher-order fractals can similarly be probed by generalising this technique. Future research will aim to investigate the potential interrelation between the symmetry properties of the moiré fractals and their implications for strong-correlation physics [88]. Additionally, it will explore the extension of the concept of moiré fractals to external potentials which lack a common moiré periodicity [89, 90], while still exhibiting fractal energy spectrum gaps due to incommensuration. It may also explore any nontrivial topological properties embedded in the measure of incommensuration introduced in this work, as well as the generic thermodynamic and transport properties of such moiré fractals.

The work of SG is supported by the Project MTR/2021/000513 funded by SERB, DST, Govt. of India. The work of DA is supported by a UGC (Govt. of India) fellowship.

Derivation of Eq. (5) from Eq. (3)

For a general 2D-Bravais lattice case, the direct lattice primitive vectors of the constituting layers $\boldsymbol{a}_1$ and $\boldsymbol{a}_2$ are not necessarily orthogonal, that is, $\boldsymbol{a}_1 \cdot \boldsymbol{a}_2 = a_1\, a_2\, \cos(\phi) \neq 0$ and also $|\boldsymbol{a}_1| \neq |\boldsymbol{a}_2|$. Therefore, the general square matrix that maps an integer pair $\{n_1, n_2\}$ to $\{m_1, m_2\}$ is given by Eq. (3) in the main text. For the present hexagonal case , $|a_1| = |a_2|$ and $\phi = 60°$, the necessary and sufficient condition for the integer solutions m_1, m_2, n_1 and n_2 demands these matrix elements to assume only rational values [59]. The commensurate angle θ_r comes out to be

$$\theta_r = \cos^{-1}\left[\frac{3q^2 - p^2}{3q^2 + p^2}\right] \tag{11}$$

where $q \geq p > 0$. As $p/q \to 0$ gives $\theta_r \to 0°$. The commensurate structures are distinguished on the basis of $\delta = \gcd(p, 3)$ and the direct lattice primitive vectors are

$$\begin{bmatrix} \boldsymbol{a}_1^c \\ \boldsymbol{a}_2^c \end{bmatrix} = \begin{bmatrix} p_1 & p_2 \\ -p_2 & p_1 + p_2 \end{bmatrix} \begin{bmatrix} \boldsymbol{a}_1 \\ \boldsymbol{a}_2 \end{bmatrix} \tag{12}$$

where $p_1 = (3q - p)/\gamma$ and $p_2 = 2p/\gamma$ for $\delta = 3$ and $p_1 = (q - p)/\gamma$ and $p_2 = (q - p)/\gamma$ for $\delta = 1$ and the quantity $\gamma = \gcd[3q + p, 3q - p]$. For both the cases $\delta = 1$ and $\delta = 3$, the two elements in first row p_1 and p_2 are positive integers $\mathbb{Z}^+$. Corresponding to direct space primitive vectors $\boldsymbol{a}_1^c$ and $\boldsymbol{a}_2^c$, the reciprocal space primitive vectors $\boldsymbol{b}_1^c$ and $\boldsymbol{b}_2^c$ are defined such that $\boldsymbol{a}_i^c \cdot \boldsymbol{b}_j^c = 2\pi\delta_{ij}\ \forall\ i, j = 1, 2..$ Then, the number L_N of the BZ hexagons of commensurate cell enclosed within the BZ of SLG formed by $\{\boldsymbol{b}_1, \boldsymbol{b}_2\}$ are given by Eq. (5), namely

$$L_N = \frac{|(\boldsymbol{b}_1 \times \boldsymbol{b}_2) \cdot \hat{\boldsymbol{z}}|}{|\boldsymbol{b}_1^c \times \boldsymbol{b}_2^c \cdot \hat{\boldsymbol{z}}|} = p_1^2 + p_2^2 + p_1\, p_2 \tag{13}$$

The metric space of coefficients p_1, p_2 with the Euclidean distance ($\mathbb{Z}^2$, Euclidean) shows the fractality in the arrangement of the coefficients p_1, p_2 in this space as shown in FIG. (.7). An irregular hexagon is formed for higher magnitudes of p_1, p_2 along with the smaller hexagons for lower magnitudes. This self-similar small irregular hexagons leads to the fractality in the metric space ($\mathbb{Z}^2$, Euclidean). We calculate the corresponding fractal dimension using the formula

$$D = \lim_{k\to\infty} \frac{\log(n_k)}{\log(2^k)} \tag{14}$$

where n_k is number of smaller polygons that completely fit inside the bigger polygon at the k^{th}-iteration. There are 3^k small irregular hexagons that fit inside the bigger irregular hexagon at the k^{th}-iteration and therefore the fractal dimension D is then given by

$$D = \frac{\ln(3)}{\ln(2)} = 1.585$$

Apart from the cases representative cases discussed in the main text the table (I) also contains few other interesting cases. The other FGs for these cases such as for q=5 and p=3 leads to the same value $N = 7$ and $\beta = 1$ as for $q = 3$ and $p = 1$ but the shift between the Dirac points in commensurate tBLG is $\Delta\boldsymbol{K} = \boldsymbol{b}_2^c$. However, the FG remains same as for $q = 3$ and $p = 1$. Infact, the mappings for the FGs corresponding to the other values of q being an odd number with $p = 1$ remains same with an increasing number of sides (n_c). Therefore, the class of commensurate structures with q being an odd number and $p = 1$ associate with the FGs having the same shape but different number of sides. If one draws a line

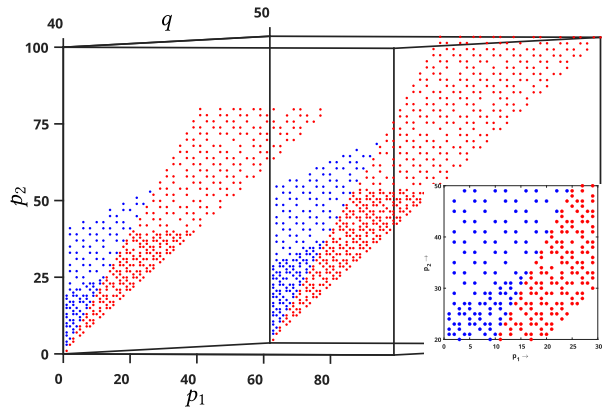

FIG. .7: It shows p_1 vs p_2 for two maximum values of q. Clearly, the points arrange themselves in hexagons and each point is associated with Löschian number.

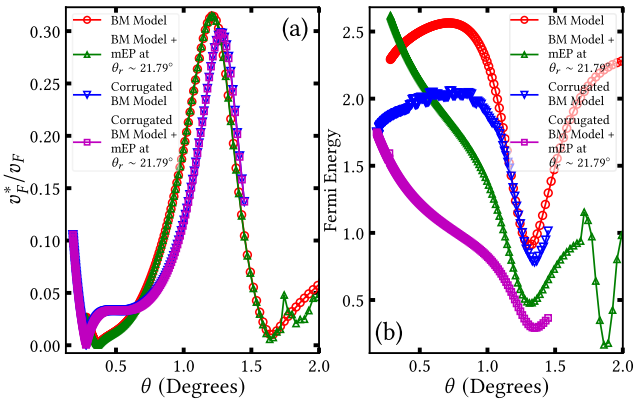

FIG. .8: The renormalized Fermi velocity v_F^*/v_F as a function of α^2 and hence the twist angle θ. The lines are just a guide to the eye.

that is perpendicular to the red dashed line in FIG. 2(a) that bisects the FG, it exactly cut it into two pieces with one becomes the other with a rotation of π in the plane containing the FG. In case of $q = 11$ and $p = 3$, the shift $\Delta\boldsymbol{K} = \boldsymbol{b}_2^c$ is same as for $q = 5$ and $p = 3$ but the FG is asymmetric about the perpendicular bisector. The corresponding FG is shown in the FIG. (.9). It shows $j = 1, 2$-level iterations in (a) and $j = 3$ in (b) Similarly, for $q = 4$ and $p = 1$, the shift in Dirac points $\Delta\boldsymbol{K} = 2\left(2\boldsymbol{b}_1^c + \boldsymbol{b}_1^c\right)/3$ is very different from the previous cases but the FG has similar shape as for $q = 2$ and $p = 1$ where the shift between Dirac points is same.

.

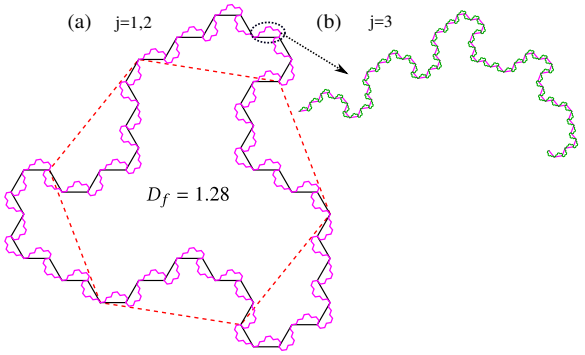

FIG. .9: The fractal corresponding to one more entry in the table where $q = 11$ and $p = 3$ having $L_N = 31$ with $\beta = 4$ at an angle of $\theta_r = 17.89°$, where (a) shows the $j = 1, 2$ iterations while (b) shows the iteration $j = 3$.

[1] B. B. Mandelbrot, *The fractal geometry of nature* (W.H. Freeman New York, 1983).

[2] J. Feder, *Fractals*, Physics of solids and liquids (Plenum Press, 1988).

[3] P. F. Duvall and L. S. Husch, Attractors of iterated function systems, Proceedings of the American Mathematical Society **116**, 279 (1992).

[4] M. F. Dacey, A note on some number properties of a hexagonal hierarchical plane lattice+, Journal of Regional Science **5**, 63 (1964), https://onlinelibrary.wiley.com/doi/pdf/10.1111/j.1467-9787.1964.tb01468.x .

[5] J. Malczewski, Central place theory, in *International Encyclopedia of Human Geography*, edited by R. Kitchin and N. Thrift (Elsevier, Oxford, 2009) pp. 26–30.

[6] J. M. B. Lopes dos Santos, N. M. R. Peres, and A. H. Castro Neto, Graphene bilayer with a twist: Electronic structure, Phys. Rev. Lett. **99**, 256802 (2007).

[7] E. Suárez Morell, J. D. Correa, P. Vargas, M. Pacheco, and Z. Barticevic, Flat bands in slightly twisted bilayer graphene: Tight-binding calculations, Phys. Rev. B **82**, 121407 (2010).

[8] G. Li, A. Luican, J. M. B. Lopes dos Santos, A. H. Castro Neto, A. Reina, J. Kong, and E. Y. Andrei, Observation of van hove singularities in twisted graphene layers, Nature Physics **6**, 109 (2010).

[9] J. Hicks, M. Sprinkle, K. Shepperd, F. Wang, A. Tejeda, A. Taleb-Ibrahimi, F. Bertran, P. Le Fèvre, W. A. de Heer, C. Berger, and E. H. Conrad, Symmetry breaking in commensurate graphene rotational stacking: Comparison of theory and experiment, Phys. Rev. B **83**, 205403 (2011).

[10] R. Bistritzer and A. H. MacDonald, Moiré bands in twisted double-layer graphene, Proceedings of the National Academy of Sciences **108**, 12233 (2011), https://www.pnas.org/content/108/30/12233.full.pdf .

[11] J. M. B. Lopes dos Santos, N. M. R. Peres, and A. H. Castro Neto, Continuum model of the twisted graphene bilayer, Phys. Rev. B **86**, 155449 (2012).

[12] C.-C. Lu, Y.-C. Lin, Z. Liu, C.-H. Yeh, K. Suenaga, and P.-W. Chiu, Twisting bilayer graphene superlattices, ACS Nano **7**, 2587 (2013).

[13] A. O. Sboychakov, A. L. Rakhmanov, A. V. Rozhkov, and F. Nori, Electronic spectrum of twisted bilayer graphene, Phys. Rev. B **92**, 075402 (2015).

[14] S. Dai, Y. Xiang, and D. J. Srolovitz, Twisted bilayer graphene: Moiré with a twist, Nano Letters **16**, 5923 (2016).

[15] Y. Cao, J. Y. Luo, V. Fatemi, S. Fang, J. D. Sanchez-Yamagishi, K. Watanabe, T. Taniguchi, E. Kaxiras, and P. Jarillo-Herrero, Superlattice-induced insulating states and valley-protected orbits in twisted bilayer graphene, Phys. Rev. Lett. **117**, 116804 (2016).

[16] M. Anđelković, L. Covaci, and F. M. Peeters, Dc conductivity

of twisted bilayer graphene: Angle-dependent transport properties and effects of disorder, Phys. Rev. Materials **2**, 034004 (2018).
[17] L. Huder, A. Artaud, T. Le Quang, G. T. de Laissardière, A. G. M. Jansen, G. Lapertot, C. Chapelier, and V. T. Renard, Electronic spectrum of twisted graphene layers under heterostrain, Phys. Rev. Lett. **120**, 156405 (2018).
[18] J.-B. Qiao, L.-J. Yin, and L. He, Twisted graphene bilayer around the first magic angle engineered by heterostrain, Phys. Rev. B **98**, 235402 (2018).
[19] L. Zou, H. C. Po, A. Vishwanath, and T. Senthil, Band structure of twisted bilayer graphene: Emergent symmetries, commensurate approximants, and wannier obstructions, Phys. Rev. B **98**, 085435 (2018).
[20] Y. Cao, V. Fatemi, S. Fang, K. Watanabe, T. Taniguchi, E. Kaxiras, and P. Jarillo-Herrero, Unconventional superconductivity in magic-angle graphene superlattices, Nature **556**, 43 (2018).
[21] Y. Cao, V. Fatemi, A. Demir, S. Fang, S. L. Tomarken, J. Y. Luo, J. D. Sanchez-Yamagishi, K. Watanabe, T. Taniguchi, E. Kaxiras, R. C. Ashoori, and P. Jarillo-Herrero, Correlated insulator behaviour at half-filling in magic-angle graphene superlattices, Nature **556**, 80 (2018).
[22] B. Lian, Z. Wang, and B. A. Bernevig, Twisted bilayer graphene: A phonon-driven superconductor, Phys. Rev. Lett. **122**, 257002 (2019).
[23] S. L. Tomarken, Y. Cao, A. Demir, K. Watanabe, T. Taniguchi, P. Jarillo-Herrero, and R. C. Ashoori, Electronic compressibility of magic-angle graphene superlattices, Phys. Rev. Lett. **123**, 046601 (2019).
[24] S. Carr, D. Massatt, S. B. Torrisi, P. Cazeaux, M. Luskin, and E. Kaxiras, Relaxation and domain formation in incommensurate two-dimensional heterostructures, Phys. Rev. B **98**, 224102 (2018).
[25] C. Kumar, S. K. Srivastav, P. Adhikary, S. Banerjee, T. Das, and A. Das, Localization physics in graphene moiré superlattices, Phys. Rev. B **98**, 155408 (2018).
[26] S. Carr, S. Fang, Z. Zhu, and E. Kaxiras, Exact continuum model for low-energy electronic states of twisted bilayer graphene, Phys. Rev. Res. **1**, 013001 (2019).
[27] E. Y. Andrei and A. H. MacDonald, Graphene bilayers with a twist, Nature Materials **19**, 1265 (2020).
[28] L. Balents, C. R. Dean, D. K. Efetov, and A. F. Young, Superconductivity and strong correlations in moiré flat bands, Nature Physics **16**, 725 (2020).
[29] U. Zondiner, A. Rozen, D. Rodan-Legrain, Y. Cao, R. Queiroz, T. Taniguchi, K. Watanabe, Y. Oreg, F. von Oppen, A. Stern, E. Berg, P. Jarillo-Herrero, and S. Ilani, Cascade of phase transitions and dirac revivals in magic-angle graphene, Nature **582**, 203 (2020).
[30] B. A. Bernevig, Z.-D. Song, N. Regnault, and B. Lian, Twisted bilayer graphene. i. matrix elements, approximations, perturbation theory, and a $k \cdot p$ two-band model, Phys. Rev. B **103**, 205411 (2021).
[31] Z.-D. Song, B. Lian, N. Regnault, and B. A. Bernevig, Twisted bilayer graphene. ii. stable symmetry anomaly, Phys. Rev. B **103**, 205412 (2021).
[32] R. Debnath, S. Sett, R. Biswas, V. Raghunathan, and A. Ghosh, A simple fabrication strategy for orientationally accurate twisted heterostructures, Nanotechnology **32**, 455705 (2021).
[33] S. M. Gardezi, H. Pirie, S. Carr, W. Dorrell, and J. E. Hoffman, Simulating twistronics in acoustic metamaterials, 2D Materials **8**, 031002 (2021).
[34] D. Aggarwal, R. Narula, and S. Ghosh, A primer on twistronics: a massless dirac fermion's journey to moiré patterns and flat bands in twisted bilayer graphene, Journal of Physics: Condensed Matter **35**, 143001 (2023).
[35] R. Hottes, Walter christaller, Annals of the Association of American Geographers **73**, 51 (1983).
[36] A. Lösch and W. Woglom, *The Economics of Location* (Yale University Press, 1954).
[37] A. Cardillo, S. Scellato, V. Latora, and S. Porta, Structural properties of planar graphs of urban street patterns, Phys. Rev. E **73**, 066107 (2006).
[38] T. Courtat, C. Gloaguen, and S. Douady, Mathematics and morphogenesis of cities: A geometrical approach, Phys. Rev. E **83**, 036106 (2011).
[39] M. Barthélemy and A. Flammini, Modeling urban street patterns, Phys. Rev. Lett. **100**, 138702 (2008).
[40] M. Barthelemy, P. Bordin, H. Berestycki, and M. Gribaudi, Self-organization versus top-down planning in the evolution of a city, Scientific Reports **3**, 2153 (2013).
[41] H. Zhang, T. Lan, and Z. Li, Fractal evolution of urban street networks in form and structure: a case study of hong kong, International Journal of Geographical Information Science **36**, 1100 (2022), https://doi.org/10.1080/13658816.2021.1974451 .
[42] D. R. Hofstadter, Energy levels and wave functions of bloch electrons in rational and irrational magnetic fields, Phys. Rev. B **14**, 2239 (1976).
[43] C. Albrecht, J. H. Smet, K. von Klitzing, D. Weiss, V. Umansky, and H. Schweizer, Evidence of hofstadter's fractal energy spectrum in the quantized hall conductance, Phys. Rev. Lett. **86**, 147 (2001).
[44] D. J. Thouless, M. Kohmoto, M. P. Nightingale, and M. den Nijs, Quantized hall conductance in a two-dimensional periodic potential, Phys. Rev. Lett. **49**, 405 (1982).
[45] M. Kohmoto, Topological invariant and the quantization of the hall conductance, Annals of Physics **160**, 343 (1985).
[46] J. U. Marshall, The löschian numbers as a problem in number theory, Geographical Analysis **7**, 421 (1975), https://onlinelibrary.wiley.com/doi/pdf/10.1111/j.1538-4632.1975.tb01054.x .
[47] K. S. Novoselov, A. K. Geim, S. V. Morozov, D. Jiang, Y. Zhang, S. V. Dubonos, I. V. Grigorieva, and A. A. Firsov, Electric field effect in atomically thin carbon films, Science **306**, 666 (2004), https://science.sciencemag.org/content/306/5696/666.full.pdf .
[48] K. S. Novoselov, D. Jiang, F. Schedin, T. J. Booth, V. V. Khotkevich, S. V. Morozov, and A. K. Geim, Two-dimensional atomic crystals, Proceedings of the National Academy of Sciences **102**, 10451 (2005), https://www.pnas.org/content/102/30/10451.full.pdf .
[49] A. K. Geim and I. V. Grigorieva, Van der waals heterostructures, Nature **499**, 419 (2013).
[50] C. Dean, A. Young, L. Wang, I. Meric, G.-H. Lee, K. Watanabe, T. Taniguchi, K. Shepard, P. Kim, and J. Hone, Graphene based heterostructures, Solid State Communications **152**, 1275 (2012), exploring Graphene, Recent Research Advances.
[51] M. Yankowitz, J. Xue, D. Cormode, J. D. Sanchez-Yamagishi, K. Watanabe, T. Taniguchi, P. Jarillo-Herrero, P. Jacquod, and B. J. LeRoy, Emergence of superlattice dirac points in graphene on hexagonal boron nitride, Nature Physics **8**, 382 (2012).
[52] J. R. Wallbank, A. A. Patel, M. Mucha-Kruczyński, A. K. Geim, and V. I. Fal'ko, Generic miniband structure of graphene on a hexagonal substrate, Phys. Rev. B **87**, 245408 (2013).
[53] P. Moon and M. Koshino, Electronic properties of graphene/hexagonal-boron-nitride moiré superlattice, Phys. Rev. B **90**, 155406 (2014).
[54] A. H. Castro Neto, F. Guinea, N. M. R. Peres, K. S. Novoselov, and A. K. Geim, The electronic properties of graphene, Rev.

Mod. Phys. **81**, 109 (2009).
[55] S. Reich, J. Maultzsch, C. Thomsen, and P. Ordejón, Tight-binding description of graphene, Phys. Rev. B **66**, 035412 (2002).
[56] R. Bistritzer and A. H. MacDonald, Transport between twisted graphene layers, Phys. Rev. B **81**, 245412 (2010).
[57] G. Tarnopolsky, A. J. Kruchkov, and A. Vishwanath, Origin of magic angles in twisted bilayer graphene, Phys. Rev. Lett. **122**, 106405 (2019).
[58] P. J. Ledwith, E. Khalaf, and A. Vishwanath, Strong coupling theory of magic-angle graphene: A pedagogical introduction, Annals of Physics **435**, 168646 (2021), special issue on Philip W. Anderson.
[59] S. Shallcross, S. Sharma, E. Kandelaki, and O. A. Pankratov, Electronic structure of turbostratic graphene, Phys. Rev. B **81**, 165105 (2010).
[60] F. Guinea and N. R. Walet, Electrostatic effects, band distortions, and superconductivity in twisted graphene bilayers, Proceedings of the National Academy of Sciences **115**, 13174 (2018), https://www.pnas.org/doi/pdf/10.1073/pnas.1810947115 .
[61] L. Rademaker, D. A. Abanin, and P. Mellado, Charge smoothening and band flattening due to hartree corrections in twisted bilayer graphene, Phys. Rev. B **100**, 205114 (2019).
[62] Z. A. H. Goodwin, V. Vitale, X. Liang, A. A. Mostofi, and J. Lischner, Hartree theory calculations of quasiparticle properties in twisted bilayer graphene, Electronic Structure **2**, 034001 (2020).
[63] J. Cao, F. Qi, H. Yang, and G. Jin, Superflat energy band induced by moiré electric potential in twisted bilayer graphene, Phys. Rev. B **103**, 165417 (2021).
[64] S. L. Arlinghaus, Fractals take a central place, Geografiska Annaler: Series B, Human Geography **67**, 83 (1985), https://doi.org/10.1080/04353684.1985.11879517 .
[65] S. L. Arlinghaus and W. C. Arlinghaus, The fractal theory of central place geometry: A diophantine analysis of fractal generators for arbitrary löschian numbers, Geographical Analysis **21**, 103 (1989), https://onlinelibrary.wiley.com/doi/pdf/10.1111/j.1538-4632.1989.tb00882.x .
[66] A. Inbar, J. Birkbeck, J. Xiao, T. Taniguchi, K. Watanabe, B. Yan, Y. Oreg, A. Stern, E. Berg, and S. Ilani, The quantum twisting microscope, Nature **614**, 682 (2023).
[67] M. Barnsley, *Fractals Everywhere*, Dover Books on Mathematics (Dover Publications, 2012).
[68] C.-H. Park, L. Yang, Y.-W. Son, M. L. Cohen, and S. G. Louie, Anisotropic behaviours of massless dirac fermions in graphene under periodic potentials, Nature Physics **4**, 213 (2008).
[69] A. H. MacDonald, Landau-level subband structure of electrons on a square lattice, Phys. Rev. B **28**, 6713 (1983).
[70] A. H. MacDonald, Quantized hall effect in a hexagonal periodic potential, Phys. Rev. B **29**, 3057 (1984).
[71] M. Koshino and P. Moon, Electronic properties of incommensurate atomic layers, Journal of the Physical Society of Japan **84**, 121001 (2015), https://doi.org/10.7566/JPSJ.84.121001 .
[72] M. Koshino, N. F. Q. Yuan, T. Koretsune, M. Ochi, K. Kuroki, and L. Fu, Maximally localized wannier orbitals and the extended hubbard model for twisted bilayer graphene, Phys. Rev. X **8**, 031087 (2018).
[73] E. J. Mele, Commensuration and interlayer coherence in twisted bilayer graphene, Phys. Rev. B **81**, 161405 (2010).
[74] K. Uchida, S. Furuya, J.-I. Iwata, and A. Oshiyama, Atomic corrugation and electron localization due to moiré patterns in twisted bilayer graphenes, Phys. Rev. B **90**, 155451 (2014).
[75] N. N. T. Nam and M. Koshino, Lattice relaxation and energy band modulation in twisted bilayer graphene, Phys. Rev. B **96**, 075311 (2017).
[76] X. Lu, P. Stepanov, W. Yang, M. Xie, M. A. Aamir, I. Das, C. Urgell, K. Watanabe, T. Taniguchi, G. Zhang, A. Bachtold, A. H. MacDonald, and D. K. Efetov, Superconductors, orbital magnets and correlated states in magic-angle bilayer graphene, Nature **574**, 653 (2019).
[77] M. Serlin, C. L. Tschirhart, H. Polshyn, Y. Zhang, J. Zhu, K. Watanabe, T. Taniguchi, L. Balents, and A. F. Young, Intrinsic quantized anomalous hall effect in a moiré heterostructure, Science **367**, 900 (2020), https://www.science.org/doi/pdf/10.1126/science.aay5533 .
[78] K. P. Nuckolls, M. Oh, D. Wong, B. Lian, K. Watanabe, T. Taniguchi, B. A. Bernevig, and A. Yazdani, Strongly correlated chern insulators in magic-angle twisted bilayer graphene, Nature **588**, 610 (2020).
[79] S. Wu, Z. Zhang, K. Watanabe, T. Taniguchi, and E. Y. Andrei, Chern insulators, van hove singularities and topological flat bands in magic-angle twisted bilayer graphene, Nature Materials **20**, 488 (2021).
[80] Y. Saito, J. Ge, L. Rademaker, K. Watanabe, T. Taniguchi, D. A. Abanin, and A. F. Young, Hofstadter subband ferromagnetism and symmetry-broken chern insulators in twisted bilayer graphene, Nature Physics **17**, 478 (2021).
[81] I. Das, X. Lu, J. Herzog-Arbeitman, Z.-D. Song, K. Watanabe, T. Taniguchi, B. A. Bernevig, and D. K. Efetov, Symmetry-broken chern insulators and rashba-like landau-level crossings in magic-angle bilayer graphene, Nature Physics **17**, 710 (2021).
[82] P. J. Ledwith, G. Tarnopolsky, E. Khalaf, and A. Vishwanath, Fractional chern insulator states in twisted bilayer graphene: An analytical approach, Phys. Rev. Research **2**, 023237 (2020).
[83] Y. Cao, D. Rodan-Legrain, J. M. Park, N. F. Q. Yuan, K. Watanabe, T. Taniguchi, R. M. Fernandes, L. Fu, and P. Jarillo-Herrero, Nematicity and competing orders in superconducting magic-angle graphene, Science **372**, 264 (2021), https://www.science.org/doi/pdf/10.1126/science.abc2836 .
[84] N. Leconte, S. Javvaji, J. An, A. Samudrala, and J. Jung, Relaxation effects in twisted bilayer graphene: A multiscale approach, Phys. Rev. B **106**, 115410 (2022).
[85] L. C. Collins, T. G. Witte, R. Silverman, D. B. Green, and K. K. Gomes, Imaging quasiperiodic electronic states in a synthetic penrose tiling, Nature Communications **8**, 15961 (2017).
[86] S. Dubey, V. Singh, A. K. Bhat, P. Parikh, S. Grover, R. Sensarma, V. Tripathi, K. Sengupta, and M. M. Deshmukh, Tunable superlattice in graphene to control the number of dirac points, Nano Letters **13**, 3990 (2013), pMID: 23937358, https://doi.org/10.1021/nl4006029 .
[87] C. Forsythe, X. Zhou, K. Watanabe, T. Taniguchi, A. Pasupathy, P. Moon, M. Koshino, P. Kim, and C. R. Dean, Band structure engineering of 2d materials using patterned dielectric superlattices, Nature Nanotechnology **13**, 566 (2018).
[88] M. Oh, K. P. Nuckolls, D. Wong, R. L. Lee, X. Liu, K. Watanabe, T. Taniguchi, and A. Yazdani, Evidence for unconventional superconductivity in twisted bilayer graphene, Nature **600**, 240 (2021).
[89] H. Oka and M. Koshino, Fractal energy gaps and topological invariants in hbn/graphene/hbn double moiré systems, Phys. Rev. B **104**, 035306 (2021).
[90] M. Koshino and H. Oka, Topological invariants in two-dimensional quasicrystals, Phys. Rev. Research **4**, 013028 (2022).